Global energy and water balance: Characteristics from Finite-volume Atmospheric Model of the IAP/LASG (FAMIL1)

Linjiong Zhou[1,2], Qing Bao[1], Yimin Liu[1], Guoxiong Wu[1], Wei-Chyung Wang[3], Xiaocong Wang[1], Bian He[1], Haiyang Yu[1], and Jiandong Li[1]

[1]State Key Laboratory of Numerical Modeling for Atmospheric Sciences and Geophysical Fluid Dynamics, Institute of Atmospheric Physics, Chinese Academy of Sciences, Beijing, China, [2]Graduate University of the Chinese Academy of Sciences, Beijing, China, [3]Atmospheric Sciences Research Center, University at Albany, State University of New York, Albany, New York, USA

Abstract This paper documents version 1 of the Finite-volume Atmospheric Model of the IAP/LASG (FAMIL1), which has a flexible horizontal resolution up to a quarter of 1°. The model, currently running on the "Tianhe 1A" supercomputer, is the atmospheric component of the third-generation Flexible Global Ocean-Atmosphere-Land climate System model (FGOALS3) which will participate in the Coupled Model Intercomparison Project Phase 6 (CMIP6). In addition to describing the dynamical core and physical parameterizations of FAMIL1, this paper describes the simulated characteristics of energy and water balances and compares them with observational/reanalysis data. The comparisons indicate that the model simulates well the seasonal and geographical distributions of radiative fluxes at the top of the atmosphere and at the surface, as well as the surface latent and sensible heat fluxes. A major weakness in the energy balance is identified in the regions where extensive and persistent marine stratocumulus is present. Analysis of the global water balance also indicates realistic seasonal and geographical distributions with the global annual mean of evaporation minus precipitation being approximately 10^{-5} mm d^{-1}. We also examine the connections between the global energy and water balance and discuss the possible link between the two within the context of the findings from the reanalysis data. Finally, the model biases as well as possible solutions are discussed.

1. Introduction

Version 1 of the Finite-volume Atmospheric Model of the Institute of Atmospheric Physics (IAP)/State Key Laboratory of Numerical Modeling for Atmospheric Sciences and Geophysical Fluid Dynamics (LASG) (FAMIL1), Chinese Academy of Sciences, is one of the newest atmospheric components of the Flexible Global Ocean-Atmosphere-Land System (FGOALS) model. The previous version of FAMIL1 is a spectral atmospheric general circulation model (AGCM) called the Spectral Atmospheric Model of the IAP/LASG (SAMIL). SAMIL has been developed from a low-resolution model (R15, approximately 400 km, in horizontal grids and nine vertical layers) to an intermediate-resolution model (R42, approximately 200 km, in horizontal grids and 26 vertical layers) [*Wu et al.*, 1996, 2003; *Wang et al.*, 2004; *Bao et al.*, 2010]. Accordingly, the interseasonal-to-decadal performances of SAMIL have been improved to some extent [*Bao et al.*, 2013; *Yang et al.*, 2013]. As with previous versions of the general circulation models (GCMs) developed by the LASG/IAP, the latest version of its AGCM, i.e., FAMIL1, is also aimed at taking active roles in most of the modeling intercomparison projects, including the Aqua Planet Experiment (APE), Atmospheric Model Intercomparison Project (AMIP), Coupled Model Intercomparison Project (CMIP), Cloud Feedback Model Intercomparison Project (CFMIP), and the scenario runs of the Intergovernmental Panel on Climate Change (IPCC). Thus, it is necessary to comprehensively evaluate the key performances of FAMIL1 before participating in these projects.

The climate system is largely regulated by the global energy and water balance and their spatial and temporal variations, which involves the flow of energy and water within the climate system and their exchanges with outer space and the surface. Spatial and temporal radiative energy imbalance is usually compensated by dynamical energy transport while the local imbalance in water fluxes (e.g., evaporation-precipitation) must be balanced by the nonlocal water vapor transport. Because the latent heat transport associated with the water fluxes is itself part of the global energy cycle, the global energy and water (hydrological) cycles

are intimately linked with the each other. Over global average, the change in the net atmospheric radiative cooling (or available radiative energy) should be balanced by corresponding changes in the latent heat release and water balance, which in turn can pose great challenges for societies and ecosystems [*Ramanathan et al.*, 2001; *Allen and Ingram*, 2002; *Lu and Cai*, 2009; *Wild and Liepert*, 2010]. Despite their central environmental and societal importance, our understanding of the causes and magnitude of the variations in the energy and water balance is still unsatisfactory [*Ramanathan et al.*, 2001; *Ohmura and Wild*, 2002; *Stephens et al.*, 2012]. Substantial uncertainties exist in the quantification of their different components, and their representation in climate models, as pointed out in numerous studies published over recent decades [*Kiehl and Trenberth*, 1997; *Trenberth et al.*, 2009; *Bengtsson*, 2010; *Stephens et al.*, 2012].

The energy and water balance of the climate system are not well understood, poorly observed, and still uncertain in GCMs [*Waliser et al.*, 2007; *Stephens et al.*, 2012; *Wild et al.*, 2013]. With the growth of global and regional observations, advances in the theoretical understanding of atmospheric, hydrospheric, cryospheric, and biospheric processes prompt the incorporation in GCMs of more physical processes, making them more complicated, but assisting in our understanding of the energy and hydrological cycle. Therefore, it becomes crucial to evaluate and understand the ability of GCMs to represent the global energy and water balance, in order to determine to what extent we can trust GCM predictions of changes in the energy and hydrological cycles under climate change scenarios.

This study evaluates the simulated global energy and water balance of the latest atmospheric model, FAMIL1, through comparisons with various satellite-based and station-based observational and reanalysis data sets, as well as the outputs of 16 CMIP Phase 5 (CMIP5)/IPCC Fifth Assessment Report (AR5) models. The work aims to answer the following questions: how well can FAMIL1 simulate both the energy and water balance? How well can FAMIL1 reproduce the connections between the energy and water balance? What are the main biases in modeled energy and water balance and their possible causes?

The remainder of the paper is organized as follows: section 2 provides a brief description of the atmospheric model. Section 3 describes the data sets used for the evaluation. Section 4 reports the performance of the simulated global energy and water balance in FAMIL1. Section 5 demonstrates the possible connections between the simulated energy and water balance in FAMIL1. And finally, further discussion and a summary of the key findings are provided in section 6.

2. Model Description and Experiments

FAMIL1 adopts the finite-volume algorithm in the module of the dynamic core; this algorithm is calculated on a cubed-sphere grid system, thus avoiding the pole issue inherent in longitude-latitude grid systems [*Lin*, 2004; *Putman and Lin*, 2007]. A flux-form semi-Lagrangian transport scheme is used to calculate the advection terms in FAMIL1, making it both stable and conservative [*Lin and Rood*, 1996; *Wang et al.*, 2013]. The model's horizontal resolution is flexible and can be changed from 200 to 25 km while the size of the grid cell varies as a factor from 0.81 to 1.16. In this study, the results from 200 km resolution are analyzed, since this resolution is the default and the most widely used resolution for the FAMIL model. The number of vertical levels in FAMIL1 has been increased to 32 (from 26 in SAMIL2), in which there are eight levels in the planetary boundary layer and 20 levels in the troposphere (see supporting information Figure S1). The uppermost level in FAMIL1 has a pressure of 2.16 hPa, a height of about 40 km for a surface pressure of 1013.25 hPa. The main computing platform of FAMIL1 is the "Tianhe-1A" supercomputer, which was one of the fastest computers in the world until very recently (http://www.top500.org/lists/2010/11/). FAMIL1 has been proven to have high computing performance in both large-scale parallel computing and effective file-Input/Output studies on the Tianhe-1A supercomputer [*Zhou et al.*, 2012].

The following physical parameterizations of FAMIL1 are the same as those in SAMIL2: the cumulus convective parameterization is based on the bulk mass-flux framework developed by *Tiedtke* [1989], in which three types of convections—penetrative convection in connection with large-scale convergent flow, shallow convections in suppressed conditions such as trade wind cumuli, and middle convection such as extratropical organized convection—are uniformly treated. In addition to the default trigging function and closure assumption in deep convection, two other variants have also been added, including those based on convective available potential energy (CAPE) [*Nordeng*, 1994], and the dynamic CAPE in which large-scale dynamics is accounted for [*Xie and Zhang*, 2000; *Zhang*, 2002; *Wang and Zhang*, 2013]. However, the

dynamic CAPE so far on is only for single-column experiments, through which the sensitivity of triggering and closure assumptions can be easily studied. For FAMIL1 and SAMIL2, the default choice is still the one proposed by *Nordeng* [1994]. The planetary boundary layer scheme of the model is a "nonlocal" first-order closure schemes determining an eddy-diffusivity profile based on a diagnosed boundary layer height and a turbulent velocity scale. It also incorporates nonlocal (vertical) transport effects for heat and moisture. This scheme represents the effects of dry convective plumes whose vertical scale is the depth of the boundary layer. Within this scheme, the boundary layer depth is calculated explicitly [*Holtslag and Boville*, 1993]. The gravity wave drag scheme considers only the topographic effect [*Palmer et al.*, 1986].

In order to improve the performance of the simulated energy and water balance, radiation, cloud microphysics, and some parameters in the convection schemes have been updated in FAMIL1, which are majorly different from SAMIL2. First, the latest version of the Rapid Radiative Transfer Model for GCMs (RRTMG) [*Clough et al.*, 2005] (http://rtweb.aer.com/rrtm_frame.html) replaced the Sun-Edwards-Slingo radiation scheme [*Edwards and Slingo*, 1996; *Sun*, 2011] in SAMIL2. RRTMG utilizes the correlated k-distribution technique to efficiently calculate the irradiance and heating rate in 14 shortwave and 16 longwave spectral intervals. The Monte-Carlo Independent Column Approximation is included into RRTMG to treat subgrid cloud overlap [*Pincus et al.*, 2003]. In addition, prescribed aerosol fields are taken from the National Center for Atmospheric Research (NCAR) Community Atmosphere Model with Chemistry (CAM-Chem) [*Lamarque et al.*, 2012]. There are five aerosol species including sulfates, sea salts, black carbon, organic carbon, and dust. In the original NCAR aerosol data set, only the bulk masses with lognormal distributions are calculated for black carbon, organic carbon, and sulfate. Four size bins are used for sea-salt and dust aerosols. The details about aerosol size parameters are provided by *Lamarque et al.* [2010], which are the standard forcings recommended by CMIP5. The aerosol data sets have a 1.9° × 2.5° horizontal resolution and a monthly temporal resolution with a seasonal cycle. Aerosol optical properties for each species follow the treatments in the version of the RRTMG radiation scheme used in NCAR CAM5 [*Ghan and Zaveri*, 2007; *Liu et al.*, 2012]. Different aerosol species are externally mixed in the radiation calculation. Then, to improve the performance of water balance, FAMIL1 implements a single moment cloud microphysics scheme, the same as that used in the Geophysical Fluid Dynamics Laboratory High Resolution Atmosphere Model (GFDL HiRAM) [*Harris and Lin*, 2014], to predict bulk contents of cloud water, rain, snow, ice crystals, and graupel/hail, instead of simple large-scale condensation processes as used in SAMIL2. The algorithms of this cloud microphysics scheme were originally based on *Lin et al.* [1983], but many key elements have been changed/improved based on several other publications [*Rutledge and Hobbs*, 1984; *Dudhia*, 1989; *Fowler et al.*, 1996; *Hong et al.*, 2004]. In the parameterization, cloud condensation nuclei (CCN) are prescribed and only the land-ocean difference of CCN is considered [*Klein and Jakob*, 1999]. These CCN is then considered as a factor to modify the generation of cloud water and cloud ice. A linear subgrid vertical distribution of cloud water and cloud ice is assumed following *Lin et al.* [1994]. Condensation happens immediately when conditions are saturated. The formula is the same as that in *Morrison et al.* [2005]. The prognostic liquid and ice equations are shown in *Fowler et al.* [1996]. With this cloud microphysics scheme, detrained cloud water and cloud ice can be transformed to other forms of water, and large-scale precipitation is explicitly calculated, and more water phases can be considered for precisely simulating the water distribution and variability. The calculation of cloud after cloud microphysics processes employs the *Xu and Randall* [1996] scheme, which considers not only relative humidity but also the cloud mixing ratio, thus providing a more precise cloud diagnosis. The cloud water and cloud ice water content needed in radiation are prognostic. Finally, all physical parameterizations are corrected to be energy and water conserved in every model column at every time step, as described in Appendix A.

After coupling with a revised version 3.5 of the Community Land Model (CLM3.5) [*Subin et al.*, 2010], standard AMIP runs [*Gates*, 1992] are carried out to evaluate the global energy and water balance. The following data forcings of AMIP are used to drive FAMIL1: the observed SST from the Hadley Centre [*Hurrell et al.*, 2008]; time-varying greenhouse gases [*Meinshausen et al.*, 2011]; solar constants [*Hartmann*, 1994]; 3-D ozone fields [*Cionni et al.*, 2011]; and five kinds of major aerosols [*Lamarque et al.*, 2012]. The standard AMIP run of FAMIL1 with monthly, daily, and hourly output has been integrated from 1975 to 2009. Different time periods of model data are extracted according to the duration of observational/reanalysis data sets for comparison.

The basic model performances of FAMIL1 show small root-mean-square errors (RMSEs), high correlations, and small standard deviation differences compared to different reanalysis data sets, as determined using

Taylor diagrams [*Taylor*, 2001] (see supporting information Figure S2). Besides, FAMIL1 can simulate zonal mean air temperature and zonal wind well, except for some biases in the stratosphere (see supporting information Figure S3). These biases may come from the deficiency of the model damping from gravity wave drag, and will be rectified when convective gravity wave drag is considered in the future. The bias of surface temperature over global land is relatively large (see supporting information Figure S4). The bias can reach 6 K over the Central Asia, and mostly −4 to 4 K in other regions.

3. Data Sets

Both observational/reanalysis and modeling data sets are used for the evaluations of the simulated global energy and water balance. The observational data sets include satellite-based products and station-based data sets. A detailed description of these data sets follows below:

The monthly data sets for energy balance analysis from 2001 to 2009 are: (1) the Clouds and Earth's Radiant Energy System-Energy Balanced and Filled (CERES-EBAF) data set [*Loeb et al.*, 2009]. This data set includes the total-sky and clear-sky longwave and shortwave radiative fluxes at the top of the atmosphere (TOA) and the Earth's surface, as well as the corresponding cloud radiative forcing. This data set has been widely used for model development and evaluation in recent years [*Donner et al.*, 2011; *Neale et al.*, 2013; *Allan et al.*, 2014]; (2) the European Centre for Medium-Range Weather Forecasts Reanalysis Interim (ERA-Interim) data set [*Dee et al.*, 2011]. This data set's global surface sensible and latent heat fluxes are employed due to a lack of global satellite observations. Their global mean values are comparable to other traditional reanalysis data sets but with better quality and higher resolution [*Berrisford et al.*, 2011].

The monthly data sets for water balance analysis from 1998 to 2007 are from: (1) the Global Precipitation Climatology Project (GPCP) [*Adler et al.*, 2003]; (2) the Climate Prediction Center (CPC) Merged Analysis of Precipitation (CMAP) [*Xie and Arkin*, 1997]; (3) the Tropical Rainfall Measuring Mission (TRMM) [*Huffman et al.*, 2007]; (4) the Objectively Analyzed Air-Sea Fluxes (OAFlux) [*Yu and Weller*, 2007]; and (5) the Advanced Microwave Scanning Radiometer Earth Observing System (EOS) (AMSR-E) [*Chelton and Wentz*, 2005] (this latter data set only covers the period from June 2002 to December 2007). Due to a lack of observations over land, we also employ some reanalysis data sets, as in *Trenberth et al.* [2011]. They are: the Modern Era Retrospective-Analysis for Research and Applications (MERRA) [*Rienecker et al.*, 2011], and ERA-Interim.

We also employed daily GPCP [*Huffman et al.*, 2001] and TRMM [*Huffman et al.*, 2007] data sets, hourly TRMM 3G68 version 6 data sets for water balance analysis from 1998 to 2007.

In this study, 16 available GCMs from CMIP5 downloaded directly from the Earth System Grid (ESG) and conducting AMIP runs are used. A list of the 16 models, along with their abbreviations and host institutions, is given in Table 1.

4. Simulation of the Energy and Water Balance

4.1. Energy Balance
4.1.1. Global Annual Mean
Over recent decades, there have been a large number of global energy balance studies [*Ramanathan*, 1987; *Kiehl and Trenberth*, 1997; *Trenberth et al.*, 2009; *Stephens et al.*, 2012; *Stevens and Schwartz*, 2012; *Wild et al.*, 2013]. Different schematic diagrams of the global energy balance are published in these papers, which often vary greatly in the numbers given therein representing the magnitudes of the energy flows in terms of global means. In this study, we present in Figure 1 all of these available results, as well as those from FAMIL1 and the chosen observational/reanalysis data sets, to show their uncertainty, and then make a clear comparison to demonstrate model performance.

Due to the utilization of different data sets and methodologies across the diverse range of literature, the energy balance at the TOA and at the surface varies considerably. In Figure 1, only those from *Stephens et al.* [2012] (hereafter S2012) and *Wild et al.* [2013] (hereafter W2013) give their uncertainty ranges, and only those from 22 CMIP5 models presented in W2013 give their maximum/minimum ranges. In most cases, the uncertainty ranges in S2012 are larger than or equal to those in W2013, and they always have maximum overlap, except for upward shortwave radiation at the TOA (FSUT), downward shortwave radiation at the

Table 1. List of the 16 CMIP5/IPCC AR5 Models Used in This Study, Together With Their Abbreviations, and Host Institutions

Modeling Groups	Institute ID	Model Name
Commonwealth Scientific and Industrial Research Organisation, Australia/Bureau of Meteorology, Australia	CSIRO-BOM	ACCESS1-0
		ACCESS1–3
Beijing Climate Center, China Meteorological Administration	BCC	BCC-CSM1-1
Canadian Centre for Climate Modelling and Analysis	CCCMA	CanAM4
National Center for Atmospheric Research	NCAR	CCSM4
Centre National de Recherches Meteorologiques/Centre Europeen de Recherche et Formation Avancees en Calcul Scientifique	CNRM-CERFACS	CNRM-CM5
Commonwealth Scientific and Industrial Research Organization in collaboration with Queensland Climate Change Centre of Excellence	CSIRO-QCCCE	CSIRO-Mk3–6-0
NOAA Geophysical Fluid Dynamics Laboratory	NOAA GFDL	GFDL-CM3
Institute for Numerical Mathematics	INM	INM-CM4
Institut Pierre-Simon Laplace	IPSL	IPSL-CM5A-MR
Japan Agency for Marine-Earth Science and Technology, Atmosphere and Ocean Research Institute (The University of Tokyo), and National Institute for Environmental Studies	MIROC	MIROC5
Max Planck Institute for Meteorology	MPI-M	MPI-ESM-LR
		MPI-ESM-MR
Meteorological Research Institute	MRI	MRI-AGCM3-2H
		MRI-CGCM3
Norwegian Climate Centre	NCC	NorESM1-M

surface (FSDS), and net shortwave radiation at the surface (FSNS), which only occupy a 50% overlap. However, the maximum/minimum ranges from the 22 models are significantly larger than either of the two uncertainty ranges in some cases, such as FSUT and upward longwave radiation at the TOA (FLUT), FSDS, upward shortwave radiation at the surface (FSUS), and downward longwave radiation at the surface (FLDS), which are approximately twofold larger, while others have no apparent differences. Greater uncertainty or maximum/minimum ranges of shortwave radiation mainly derive from absorbed and reflected shortwave
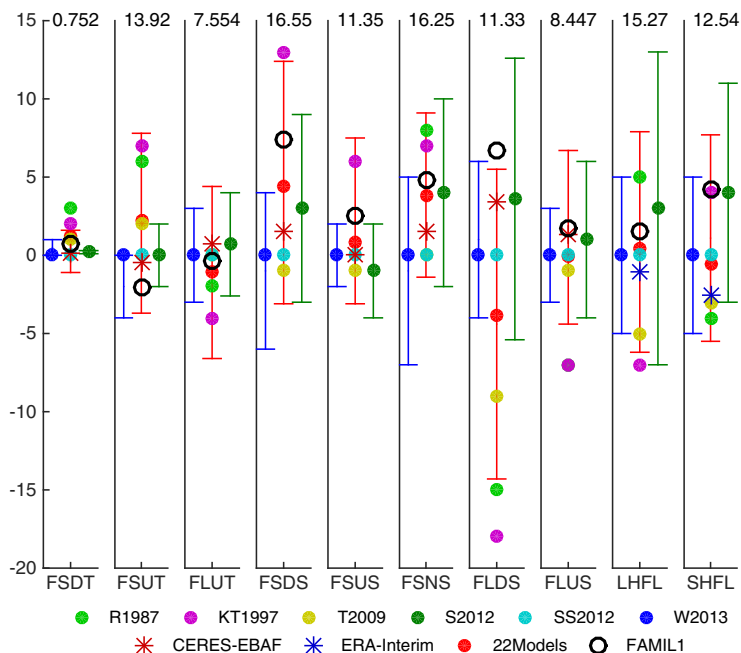

Figure 1. Global annual mean energy balance at the TOA and surface, subjectively determined based on a review of the existing literature as well as calculated from FAMIL1 and observational/reanalysis data sets (including CERES-EBAF and ERA-Interim). References to prior estimates are: R1987, KT1997, T2009, S2012, SS2012, and W2013. Green error bars indicate the uncertainty ranges from S2012. Blue error bars indicate the uncertainty ranges from W2013. Red error bars indicate the maximum/minimum ranges from 22 CMIP5/IPCC AR5 models in W2013. Units: W m^{-2}. Axis intervals are scaled to subtract the estimates from W2013. RMSEs of CERES-EBAF or ERA-Interim are listed at top of each column. (FSDT: downward shortwave radiation at TOA; FSUT: upward shortwave radiation at TOA; FLUT: upward longwave radiation at TOA; FSDS: downward shortwave radiation at the surface; FSUS: upward shortwave radiation at the surface; FSNS: net shortwave radiation at the surface; FLDS: downward longwave radiation at the surface; FLUS: upward longwave radiation at the surface; LHFL: surface latent heat flux; SHFL: surface sensible heat flux.)
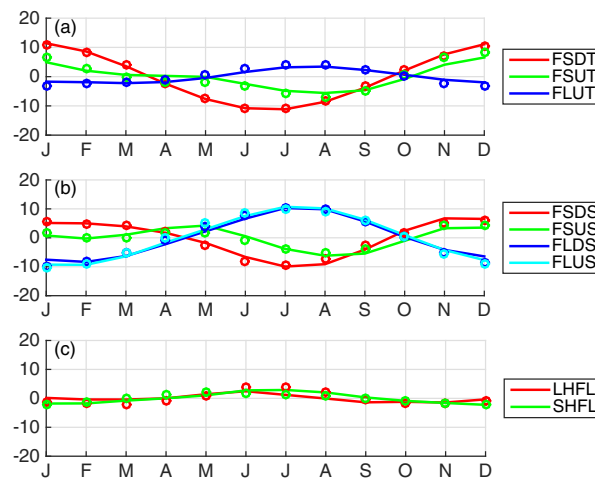
Figure 2. Seasonal cycle of global mean radiation at (a) TOA and (b) the surface from FAMIL1 (lines) and CERES-EBAF (circles); and for global mean (c) surface latent and sensible heat flux from FAMIL1 (lines) and ERA-Interim (circles). Axis intervals are scaled to subtract their annual mean values. Units: W m^{-2}. The meanings of abbreviations are the same as in Figure 1.

radiation bias in the atmosphere. This bias mainly comes from the uncertainty of cloud fraction, cloud optical properties, water vapor, and absorbing aerosol errors in the climate model. With regard to longwave radiation, both FLUT and FLDS are most related to the altitude and optical thickness of clouds and the opacity of water vapor in the atmosphere, which are also uncertain in GCMs.

Figure 1 also shows that the energy balance of the surface is spread wider than that at the TOA. The reason is that radiative fluxes at the surface have to be inferred from the measurable TOA radiances using empirical or physical models to account for atmospheric attenuation and emission, which 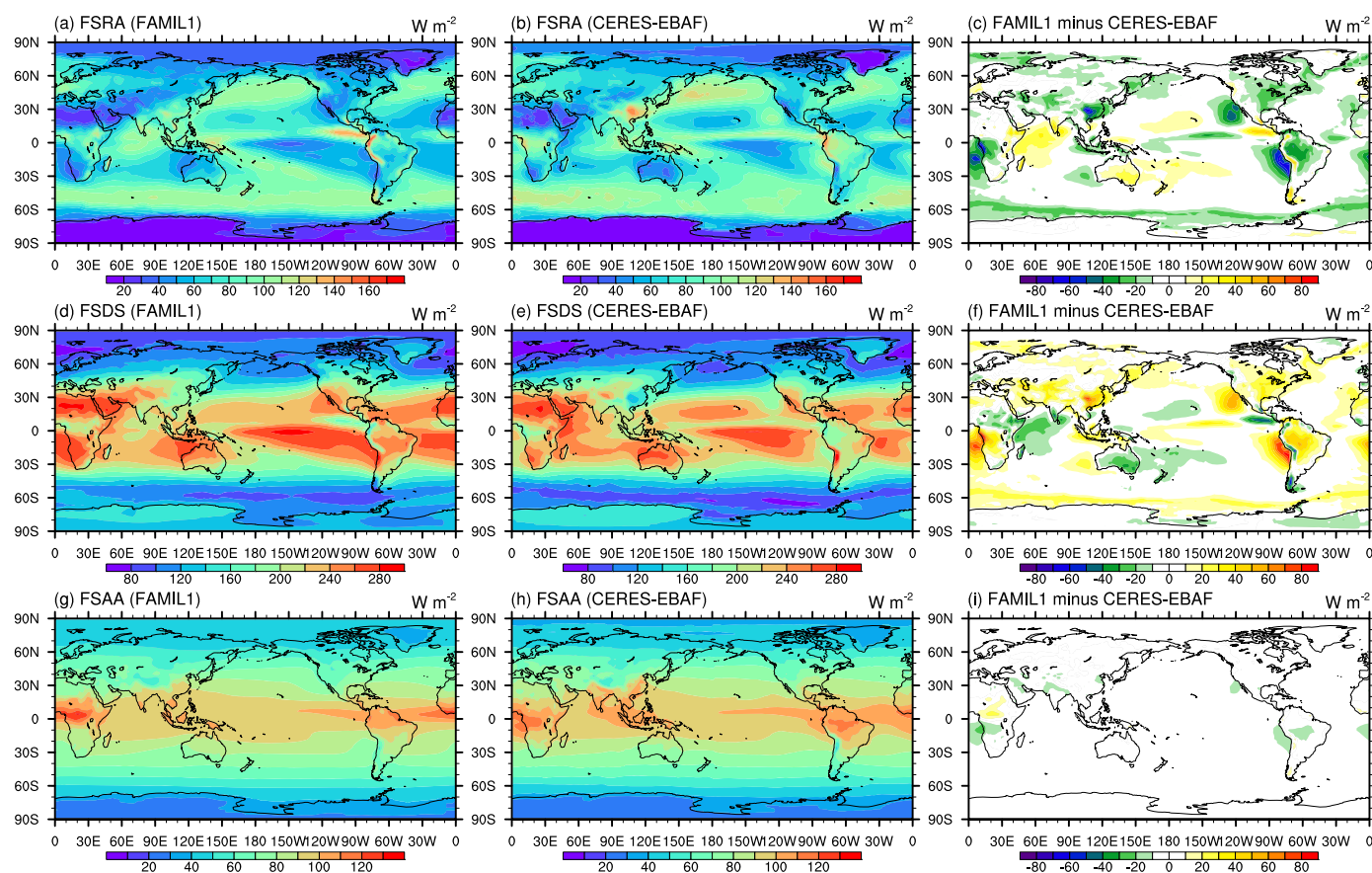introduces additional uncertainties [*Zhang et al.*, 2007; *Wild et al.*, 2013]. Within the surface energy balance, FLDS spreads the most, especially with respect to the early studies of *Ramanathan* [1987], *Kiehl and Trenberth* [1997], and *Trenberth et al.* [2009]. It has long been argued that the atmospheric emission of thermal radiation back to the Earth's surface may be too low. This flux (also known in short as (thermal) back-radiation) is central to the climate change discussion, as it immediately responds to enhance greenhouse gas concentrations, and thus dictates the greenhouse effect experienced at the Earth's surface [*Wild*, 2012]. On the other hand, it may also be related to the underestimation of precipitation and the neglected contribution from snowfall to global precipitation in the previous studies [*Stephens et al.*, 2012].

Comparing the energy balances and their uncertainty ranges from different studies with the simulation of the energy balance from FAMIL1, we see that FAMIL1 simulates the global mean energy balance reasonably. All energy fluxes from FAMIL1 are located within the uncertainty ranges of either S2012 or W2013, or both, except the FSUS, which is slightly larger. This bias mainly comes from the excessive FSDS and slightly stronger surface albedo. Nevertheless, this value is located within the maximum/minimum range of the 22 models and is lower than the estimated value from *Kiehl and Trenberth* [1997] (hereafter KT1997). Note that the FLDS is larger than any other results, although it is still located within the uncertainty ranges. This bias, as well as the excessive FSDS, is further discussed later in the paper. Global annual mean radiative fluxes from CERES-EBAF, surface sensible, and latent heat from ERA-Interim, as well as the RMSE of FAMIL1, are also shown on Figure 1, in which the relatively high RMSEs indicate salient difference between CERES-EBAF and our model result.

4.1.2. Seasonal Cycle
To obtain a better understanding of the capability of FAMIL1 in simulating the energy balance, we now focus on the seasonal cycle of the energy fluxes through the TOA and at the surface. In this section, the CERES-EBAF data set is used for comparison at the TOA and at the surface, except for surface latent and sensible heat fluxes the ERA-Interim data set is used.

Figure 2 shows the seasonal cycle for the global mean energy balance of FAMIL1 and the observational/reanalysis data sets. In general, the global-averaged shortwave radiation is weak during boreal summer and strong during boreal winter, following the variation of the FSDT, which is related to the seasonal variation of solar-Earth distance. Note that there is another radiation peak in the seasonal cycle of the FSUS, located in the April-May-June season. In this season, although the FSDT is decreasing, the declination of the sun is moving northward from the Equator leading to an increasing of the ice fraction and thickness around Antarctica, which increases the reflected upward solar radiation. On the contrary, the FLUT, FLDS, and FLUS are strong during boreal summer and weak during boreal winter. The seasonal variations of surface latent and sensible heat (LHFL and SHFL) are similar to longwave radiation with weaker amplitude.

Figure 3. Geographical distribution of reflected shortwave radiation in the atmosphere (FSRA) (top), downward shortwave radiation at the surface (FSDS) (middle), and absorbed short-wave radiation in the atmosphere (FSAA) (bottom).

As shown in Figure 2, the seasonal cycles of the energy balance of FAMIL1 are in good agreement with the different data sets used for comparison, albeit with some degrees of difference between the observational/reanalysis data sets. In general, FAMIL1 can reasonably simulate not only the seasonal cycle of the energy balance, but also its amplitude.

4.1.3. Geographical Distribution

Global mean fluxes of energy are important in describing the total energy balance of the whole atmosphere. However, the climate system is forced by the 3-D distribution of energy. Furthermore, the global mean may mask regional biases in energy fluxes. Thus, to better understand the FAMIL1 global energy balance, we present the geophysical distribution of various energy fluxes in this part.

TOA downward shortwave radiation can be divided into three parts: absorbed shortwave radiation in the atmosphere (FSAA); reflected shortwave radiation in the atmosphere (FSRA); and downward shortwave radiation at the surface (FSDS). Generally, FSAA and FSRA are smaller (23.2% and 22.4%, respectively) compared to FSDS to the Earth's surface (54.4%). The geographical distributions of these three components in FAMIL1 and CERES-EBAF are illustrated in Figure 3. The annual mean FSAA of FAMIL1 shows excellent agreement with CERES-EBAF data, with differences of almost less than 10 W m^{-2} (Figures 3g–3i), meaning the absorbed properties of aerosol and cloud are reasonable in the atmosphere. Comparing the FSRA (Figures 3d–3f), it is found that over most of the land area and the eastern ocean, solar reflection by the atmosphere in FAMIL1 is weaker than that in CERESEBAF while over the western Indian Ocean and subtropical Pacific Ocean it is stronger. Correspondingly, FSDS has the same bias but with an opposite sign. Remembering that the global annual mean FSDS is larger than that estimated from different literature sources, this positive difference mainly derives from weaker FSRA, especially the significant bias over the eastern ocean and Asia (Figures 3a–3c).

The bias can be further verified, albeit with some differences, from the TOA shortwave cloud radiative forcing (SWCRF) (Figures 4a–4c). Over the eastern ocean, weaker SWCRF is consistent with those found in
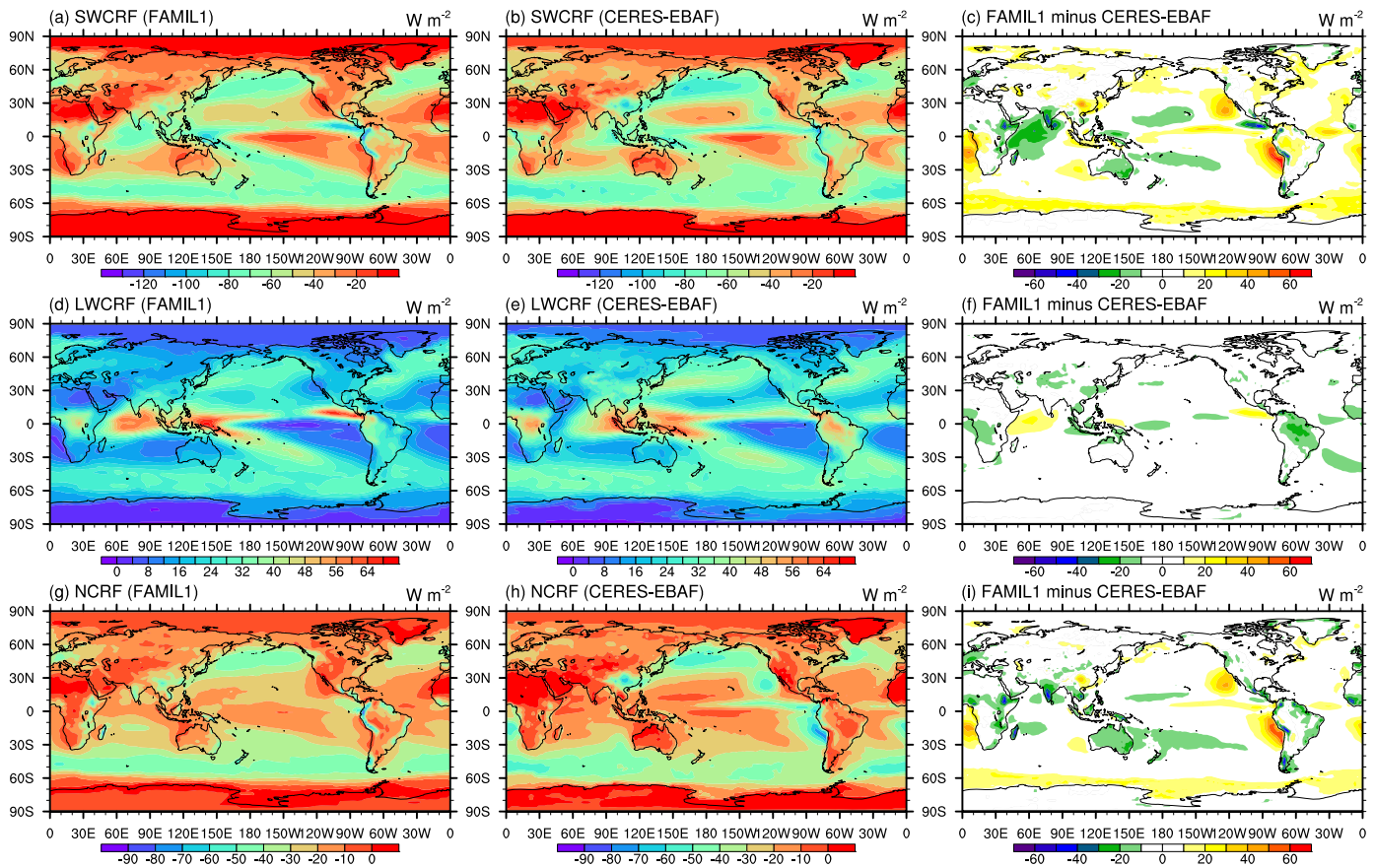
Figure 4. Geographical distribution of TOA shortwave cloud radiative forcing (SWCRF) (top), TOA longwave cloud radiative forcing (LWCRF) (middle), and TOA net cloud radiative forcing (NCRF) (bottom).

Figure 3. This bias is strongly connected to the underestimation of low-level cloud fraction (Figures 5e and 5f) calculated from the Cloud Feedback Model Intercomparison Project's Observation Simulator Package (COSP) [*Bodas-Salcedo et al.*, 2011]. With an underestimation of low-level cloud fraction, the reflection of shortwave radiation becomes weaker, and more solar radiation can reach the surface. Meanwhile, we do not see significant longwave cloud radiative forcing (LWCRF) bias over this region (Figures 4d–4f), which is also consistent with its well-simulated high-level and middle-level cloud fraction (Figures 5a–5d). In Figures 4d–4f, it is clear that LWCRF is simulated well globally. Therefore, the pattern of net cloud radiative forcing (NCRF) is similar to SWCRF, except in the western Indian Ocean (Figures 5g–5i). The stronger SWCRF over the western Indian Ocean is consistent with the weaker downward shortwave radiation at the surface and stronger reflection; but in LWCRF, it is slightly opposite. This bias may mainly derive from the excessive convection (see the next section) over this region. One possible mechanism involved is that excessive convection produces thicker cloud and larger ice water path and hence reflecting more incoming shortwave radiation [*De León et al.*, 2012]. Meanwhile, excessive convection induces more high cloud (Figures 5a and 5b), leading to more warming effect and downward longwave radiation. The same bias exists in the upward longwave radiation at the TOA (Figures 6a–6c). Since FAMIL1 has a positive water vapor bias over the global ocean (discussed in the next section), downward longwave radiation at the surface is larger than that from CERES-EBAF (Figures 6d–6f).

4.2. Water Balance
4.2.1. Global Annual Mean
Water vapor is a dominant greenhouse gas and is responsible for a major feedback process in the climate system [*Karl and Trenberth*, 2003]. In this section, we investigate two components of the water balance, precipitation, and evaporation (including evaporation, sublimation, evapotranspiration etc.), from the
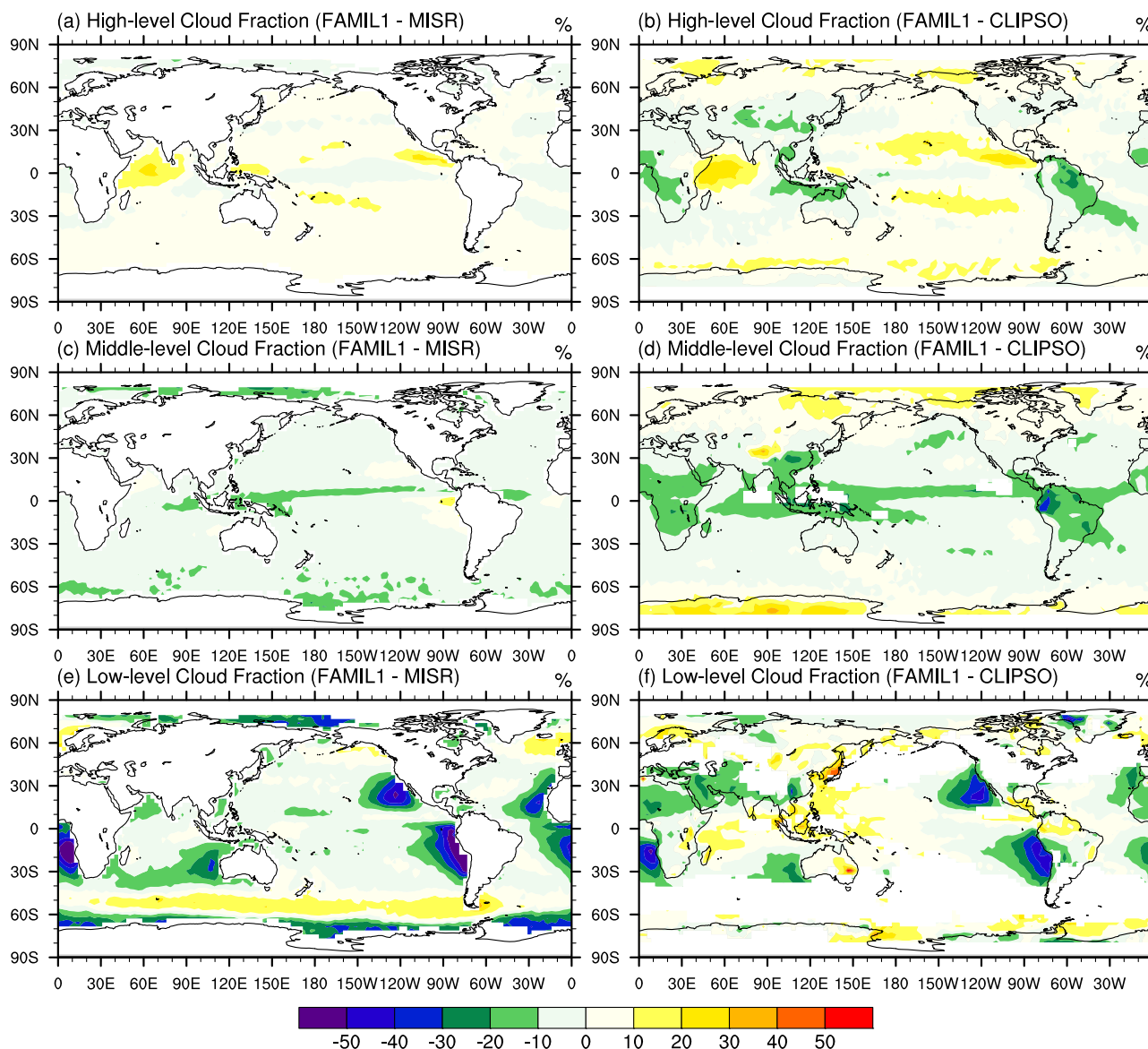
Figure 5. Annual mean geographical distribution of cloud fraction bias compared with MISR (left) and CALIPSO (right) from COSP in FAMIL1.

perspective of the global annual mean, spatial correlation, and geographical distribution, to illustrate the performance of FAMIL1 in simulating the water balance.

We employ several frequently used precipitation and evaporation data sets for the comparison between model and observations; namely, the GPCP, CMAP, TRMM, OAFlux, ERA-Interim, and MERRA data sets. In addition, data from 16 CMIP5 models (Table 1) are also used for analysis. The global annual mean precipitation, evaporation, and evaporation minus precipitation (E − P) are listed in Table 2. Overall, precipitation in FAMIL1 is greater than those in GPCP and CMAP, both of which are less than 2.7 mm d^{-1}. Excess precipitation is also apparent in ERA-Interim, MERRA, and the 16 CMIP5 models. Precipitation in FAMIL1, and the 16 CMIP models ranges from 2.9 to 3 mm d^{-1}. Since evaporation estimates over land suffer from great difficulties [*Trenberth et al.*, 2011], there is no observational data set containing global evaporation, so only ERA-Interim and MERRA are used for comparison. The behavior of evaporation between reanalysis data sets is largely different. Global mean evaporation in MERRA is less than 2.7 mm d^{-1}, but more than 2.9 mm d^{-1} in ERA-Interim. Regarding E − P, it is generally not closed in reanalysis data sets owing to the analysis increment arising from errors in the state variable fields and observational uncertainties [*Trenberth et al.*, 2011], the water imbalance of ERA-Interim, and MERRA is 0.054 and −0.111 mm d^{-1}, respectively. The 16-model
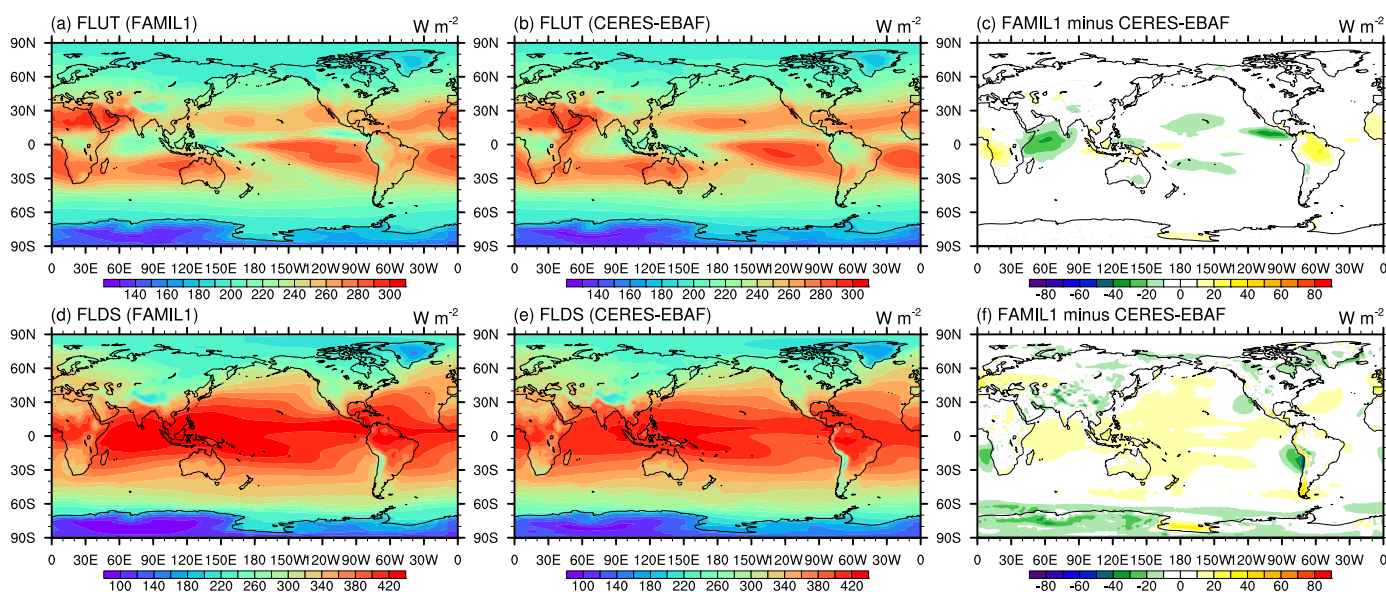
Figure 6. Geographical distribution of upward longwave radiation at TOA (FLUT) (top), and downward longwave radiation at the surface (FLDS) (bottom).

mean is -0.001 mm d^{-1}. However, in FAMIL1, it is as low as 10^{-5} mm d^{-1}. This means that almost no significant extra water source or sink is generated in terms of the FAMIL1 climatology.

4.2.2. Seasonal Cycle

Employing multiple data set sources, we further investigate the seasonal cycle of the water balance, as depicted in Figure 7. Different to the energy balance, there is larger uncertainty in the seasonal variability of the water balance among the observational and reanalysis data sets. For precipitation, the result from MERRA shows the largest amplitude, with a range of 0.2 mm d^{-1}; while that from GPCP has the smallest amplitude, with a range of no more than 0.1 mm d^{-1}. The amplitudes of CMAP and GPCP lie between the former two ranges. The variability of ERA-Interim is close to CMAP. The precipitation peaks in all of the observational/reanalysis data sets lie in boreal summer and winter while the valleys lie in spring and autumn. Precipitation in the 16 CMIP5 models is similar to that in the CMAP data, except for a 1 month phase lead. Precipitation in FAMIL1 lies within the envelope of the 16 CMIP5 models and is quite similar to the result from the multimodel mean while the amplitude of the FAMIL1 seasonal cycle is slightly weaker than observations within a range of 0.1 mm d^{-1}. For evaporation, only the results from MERRA, ERA-Interim, and the 16 CMIP5 models are presented. The result from FAMIL1 is also similar to the mean of the 16 CMIP5 models, but is smoother. The variation of evaporation is similar to that of precipitation, in spite of fewer observational/reanalysis data sets used for comparison. The degree of similarity between FAMIL1 and the 16 CMIP5 models' E − P variabilities is higher than for either precipitation or evaporation, although its magnitude and maximum/minimum range is very small. There is increasing positive E − P from January to June, a rapid decrease from positive in June to negative in September, and then an increase from September to January with negative sign.

4.2.3. Spatial Correlation

A scatterplot is employed to illustrate the spatial relation between FAMIL1 and the different observational data sets (Figure 8). Using the criterion of an annual mean value less than 5 mm d^{-1}, precipitation in

Table 2. Global Annual Mean Precipitation, Evaporation, and E − P (Evaporation Minus Precipitation) at the Surface From FAMIL1, GPCP, CMAP, EAR-Interim, MERRA, and 16 CMIP5/IPCC AR5 Models[a]

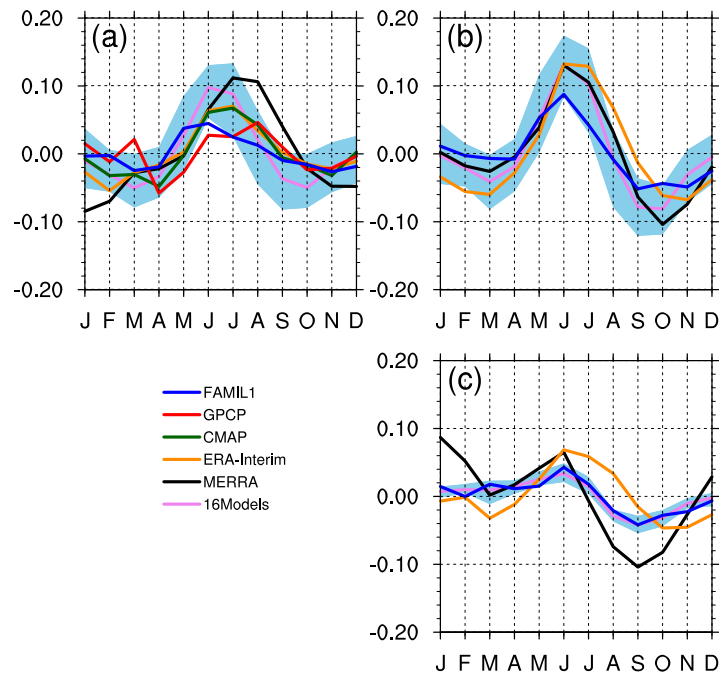| Field	FAMIL1	GPCP	CMAP	ERA-Interim	MERRA	16 Models
Prec.	2.986	2.692	2.653	2.848	2.793	2.987
Evap.	2.986			2.902	2.682	2.986
E − P	−0.000			0.054	−0.111	−0.001

[a]Units: mm d^{-1}.

Figure 7. Seasonal cycle of global mean (a) precipitation, (b) evaporation, and (c) evaporation minus precipitation from FAMIL1, GPCP, CMAP, ERA-Interim, MERRA, and data from 16 CMIP5/IPCC AR5 models. Units: mm d^{-1}. Axis intervals are scaled to subtract their annual mean values. Shaded area is the maximum/minimum range of 16 CMIP5/IPCC AR5 models.

FAMIL1 shows excellent agreement with the observational data sets. However, when the annual mean precipitation increases to more than 5 mm d^{-1}, the relation is not so robust. The frequency of extreme evaporation is much less than that of extreme precipitation, with the former being no more than 7 mm d^{-1} and the latter reaching 12 mm d^{-1}. Figure 8 also shows that evaporation from FAMIL1 agrees well with that from the observational data sets below 5 mm d^{-1}. However, when evaporation increases to more than 5 mm d^{-1}, it is significantly overestimated by FAMIL1. Overall, the simulation of evaporation is much better than precipitation in FAMIL1.

Figure 9 shows frequency versus daily precipitation and evaporation between 50°N and 50°S. FAMIL1 has far too much weak precipitation events (less than 20 mm d^{-1}) and too few strong precipitation events (between 20 and 60 mm d^{-1}) compared to observations. This
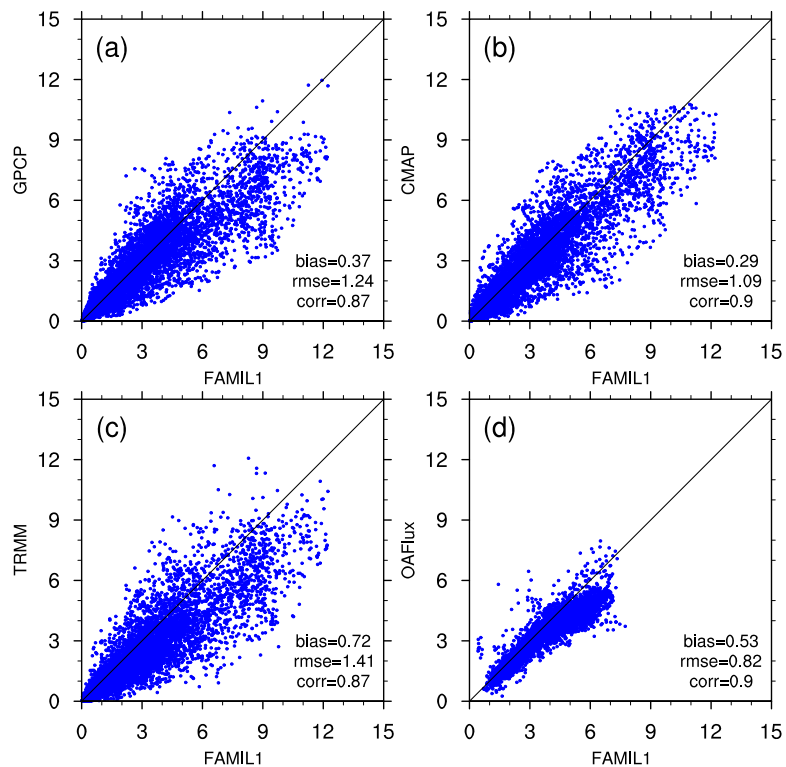

Figure 8. Comparison of annual mean precipitation between FAMIL1 and (a) GPCP, (b) CMAP, and (c) TRMM. Evaporation between FAMIL1 and (d) OAFlux. Units: mm d^{-1}. Each point represents the annual mean value in one grid box.
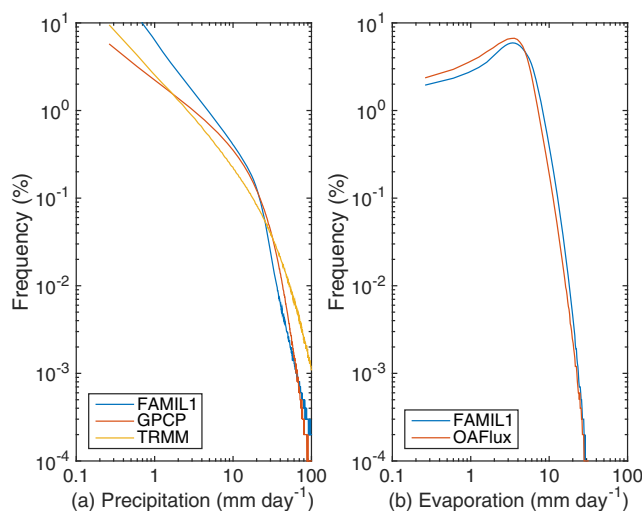
Figure 9. Frequency (%) of daily (a) precipitation and (b) evaporation between 50°N and 50°S from FAMIL1, GPCP, TRMM, and OAFlux. All data are interpolated to the 2° FAMIL1 grid. Evaporation over land is masked to match OAFlux data.

bias as further demonstrated in the next section when discussing the geographical distribution may result from the too easy triggering of convection associated with the convective parameterization. The simulated evaporation is generally acceptable. A significant shift from weak evaporation to strong evaporation appears in the simulation of FAMIL1. Compared with OAFlux, FAMIL1 can capture the peak at 4 mm d^{-1}, but its frequency is lower, indicating a total overestimation of evaporation in FAMIL1 and this will be further seen in the next section.

4.2.4. Geographical Distribution
It is very important to investigate the geographical distribution of the precipitation and evaporation components of water balance to evaluate model performance, and identify regional bias. In this section, we compare the model results with only four observational data sets: GPCP, CMAP, TRMM, and OAFlux.

Compared with the observational precipitation distribution (Figures 10a–10d), FAMIL1 can successfully simulate the global precipitation pattern, but with some bias. FAMIL1 overestimates precipitation over the western Indian Ocean, over the western Pacific Ocean (especially near the New Guinea Island). Meanwhile, there is stronger precipitation over the Himalayan Mountains and Andes, mainly due to the unrealistic depiction of the topography. It also simulates excessive precipitation over the equatorial eastern Pacific Ocean. And last, FAMIL1 underestimates precipitation over the Amazon and the equatorial Atlantic Ocean. In particular, FAMIL1 overestimates the precipitation over the southern Pacific Ocean near the Equator, which is representative of the double Intertropical Convergence Zone (ITCZ) problem that is in common among many current models [*Donner et al.*, 2011; *Neale et al.*, 2013; *Popke et al.*, 2013]. The cause of the double ITCZ bias is not clear but it is consistent with the excessive shortwave radiation to the surface over the southeastern Pacific Ocean as *Hwang and Frierson* [2013] have suggested. The overestimation of precipitation must be associated with an overestimation of evaporation. In Figures 10e and 10f, although the global pattern of evaporation is simulated well, the magnitude is higher, especially over the subtropical region in both hemispheres. In the long-term integration, FAMIL1 results in excessive water vapor in the atmosphere (Figure 11). And this is more significant over the western Indian Ocean. Water vapor is overestimated globally, except in the eastern ocean region, where low-level cloud is also underestimated (Figures 5e and 5f).

Furthermore, the diurnal cycle of precipitation from FAMIL1 is investigated following the idea of *Bechtold et al.* [2013]. Figure 12 shows the diurnal amplitude (mm d^{-1}) and phase (LST: Local Standard Time) of the precipitation from FAMIL1 and TRMM. It is found that FAMIL1 can realistically capture the spatial variations in the diurnal amplitude but fails to simulate the diurnal phase, which appears to be nearly 4–5 h earlier. Previous study on global model, regional model, and cloud-resolving model pointed to systematic errors in the diurnal cycle of precipitation when a too-early onset of deep convection parameterization scheme is employed [*Bechtold et al.*, 2013].

5. Connections Between the Energy and Water Balance

The connections between the energy and water balance have long been discussed [*Trenberth et al.*, 2011]. In this paper, the connections between the energy and water balance simulated in FAMIL1 are compared to those in the ERA-Interim reanalysis data set are evaluated.

Figures 13a and 13c show the longwave radiation cloud forcing (LWCRF) connected with precipitation and evaporation combined. From the ERA-Interim reanalysis data, we find that LWCRF increases when
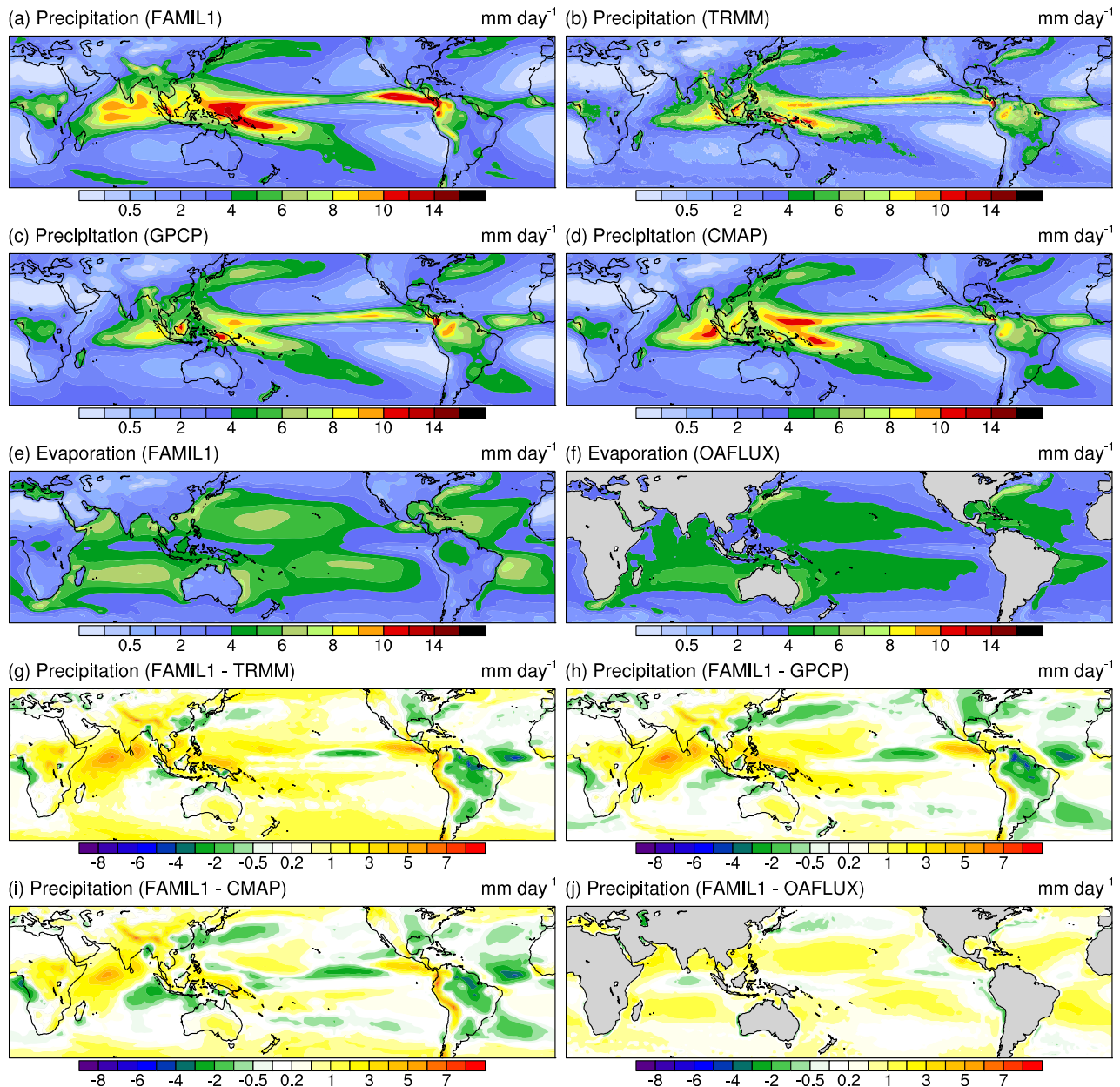
Figure 10. Geographical distribution of annual mean precipitation of (a) FAMIL1, (b) TRMM, (c) GPCP, (d) CMAP, and evaporation of (e) FAMIL1, (f) OAFLUX, and (g–j) their differences.

precipitation increases while there is no evident link between LWCRF and evaporation. The weakest (less than 10 W m^{-2}) LWCRF occurs where precipitation is weak (less than 1.5 mm d^{-1}) while the strongest LWCRF (greater than 50 W m^{-2}) occurs where precipitation is strong (greater than 7 mm d^{-1}). In most areas, LWCRF is not related to evaporation, but is strongly connected to precipitation. The performance of FAMIL1 is similar to that of ERA-Interim in this relationship, although some mismatches of precipitation/evaporation are apparent in the form of evaporation surpassing precipitation and too strong evaporation.

Figures 13b and 13d show the connection between LWCRF and the E − P and vertical motion combined. From the ERA-Interim reanalysis data, we find that strong LWCRF lies in the area where precipitation and updraft dominate while weak LWCRF lies in the area where evaporation and subsidence dominate. Such a relationship between LWCRF and vertical velocity is also documented in *Wang et al.* [2012] under aquaplanet configuration. As precipitation and updraft become stronger, LWCRF also becomes stronger. However, we also see that this relationship is not significant over most of the land area, and the relation is more
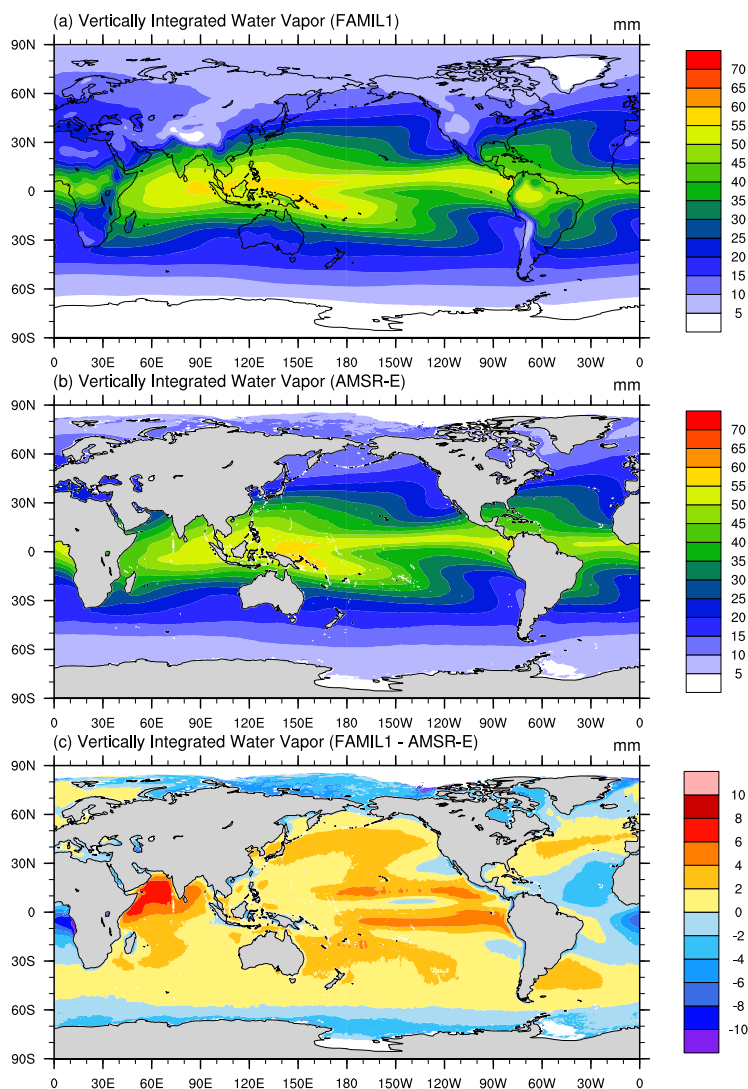
Figure 11. Geographical annual mean vertically integrated water vapor of (a) FAMIL1, (b) AMSR-E, and (c) FAMIL1 minus AMSR-E.

robust over the tropics (figure not shown). In general, the results from FAMIL1 are consistent with those from ERA-Interim.

6. Conclusions and Discussion

In this paper, the global energy and water balance simulated by FAMIL1 is evaluated using multiple sources from both the literature and comprehensive observational/reanalysis data sets. Highlights of the comparisons are summarized below and further development discussed.

In general, the global annual mean solar, longwave, sensible, and latent heat are within the uncertainty ranges of either S2012 or W2013, or both. One term, surface solar upward radiative flux, shows a slightly larger bias that is attributable to the excessive surface solar downward radiative flux and slightly stronger surface albedo. Nevertheless, this value is still within the range of 22 CMIP5 models and lower than the estimated value from KT1997. When comparing the seasonal cycle of the annual energy balance, FAMIL1 can simulate well both the seasonal cycle and amplitudes of the energy balance. It is also found that, when compared with CERESEBAF, FAMIL1 performs excellently at the TOA in terms of spatial distribution. In order to further investigate the bias found in the global annual mean, the geographical distribution of the energy balance is analyzed. It is found that over most of the land area and the eastern ocean, solar reflection by the atmosphere in FAMIL1 is weaker than that in CERES-EBAF while over the western Indian Ocean it is stronger.
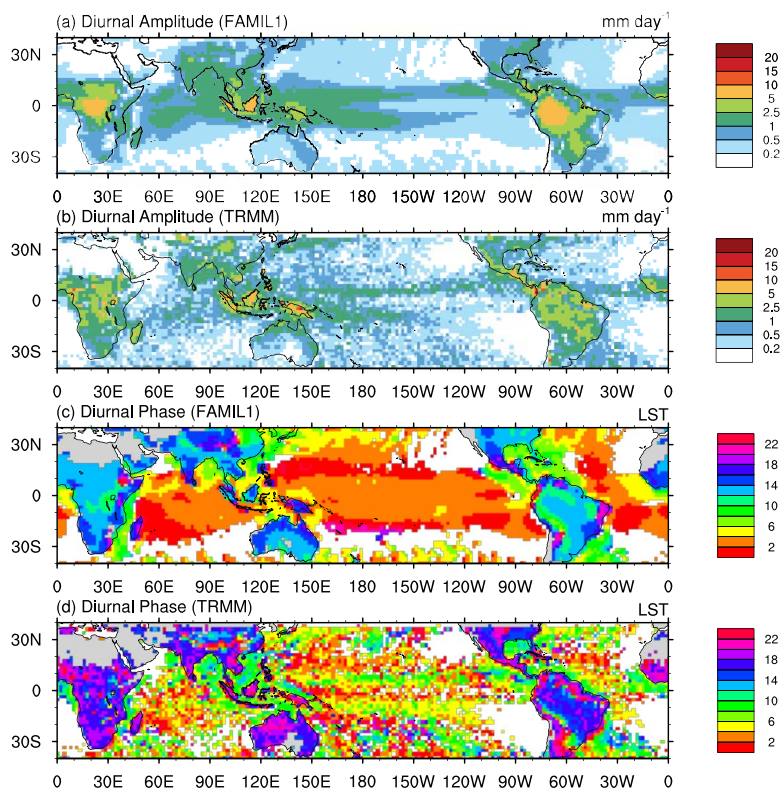
Figure 12. Diurnal amplitude (mm d^{-1}) of the precipitation in the tropical band as obtained (a) from TRMM 3G68, and (b) from FAMIL1. Diurnal phase (LST: Local Standard Time) of the precipitation in the tropical band as obtained (c) from TRMM 3G68, and (d) from FAMIL1. While shading is applied for areas where the amplitude of precipitation is below 0.2 mm d^{-1}.

Correspondingly, surface solar downward radiation shows the same bias, but with an opposite sign. Further analysis reveals that, over the eastern ocean, shortwave cloud radiation forcing is weaker. This bias is strongly connected to the underestimation of low-level cloud. On the contrary, FAMIL can better simulate longwave radiation to some extent.

We further focus on the global water balance and find that the global annual mean of E − P in FAMIL1 is approximately 10^{-5} mm d^{-1}, which is comparable with 16 CMIP5 models as well as observational/reanalysis data sets. The global seasonal cycles of precipitation, evaporation, and E − P can be realistically simulated, and in particular show good agreement with the results from 16 CMIP5 models, in spite of smoother variation. The global geographical distribution of precipitation and evaporation are fairly comparable with observations according to scatterplot analysis and intensity frequency analysis. Furthermore, FAMIL1 can realistically capture the spatial precipitation variations in the diurnal amplitude but fails to simulate the diurnal phase.

Finally, we investigate the connections between the energy balance and water balance to depict the performance of FAMIL1. It is found that FAMIL1's performance compare well with that of ERA-Interim in terms of the relationship between LWCRF and precipitation and evaporation combined, albeit with some mismatches in the form of evaporation surpassing precipitation and too strong evaporation. FAMIL1 also performs well with respect to the relationship between LWCRF and E − P and vertical motion combined.

In conclusion, FAMIL1, the latest atmospheric model developed at the IAP/LASG, performs well in terms of its simulation of the energy and water balance, as established by examining its spatiotemporal features. However, the model still has some weakness related to the simulation of clouds. This study shows large cloud bias over the East Asia and eastern ocean regions, which alters the local and global energy balance. East Asia is one of the most populous and rapidly developing regions of the globe, and has a large atmospheric loading of anthropogenic aerosols because of its rapid industrialization, urbanization, and domestic heating [*Huang et al.*, 2006]. The importance of aerosol-cloud interactions to the climate over East Asia
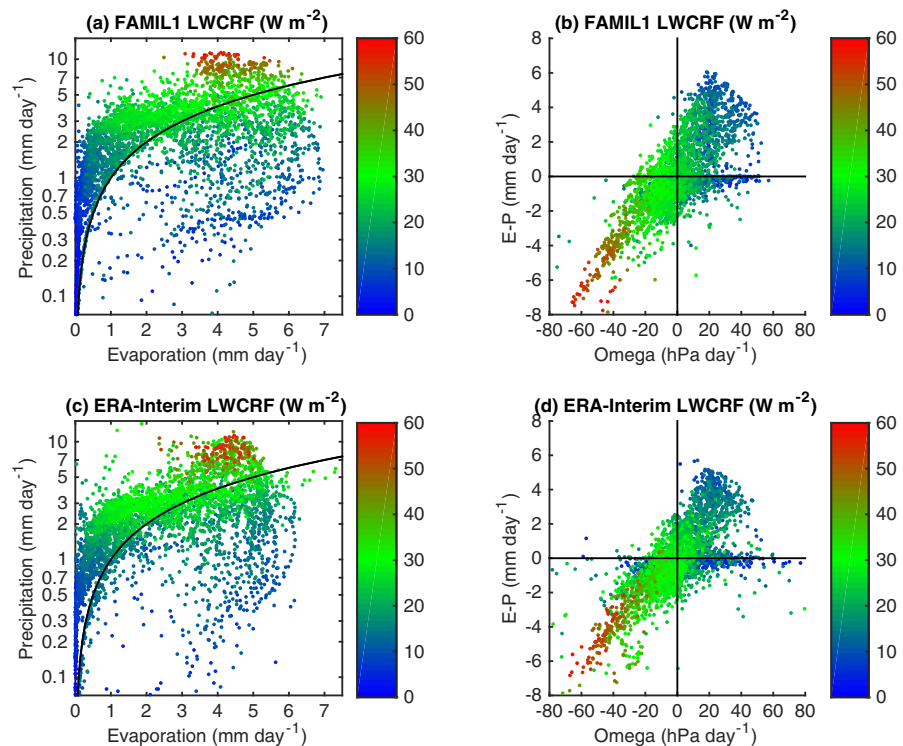
Figure 13. Annual mean distribution of TOA longwave cloud radiative forcing (LWCRF) (W m^{-2}) connected with precipitation (mm d^{-1}) and evaporation (mm d^{-1}) from (a) FAMIL1 and (c) ERA-Interim; and evaporation minus precipitation (E − P) (mm d^{-1}) and vertical motion (Omega) (hPa d^{-1}) from (b) FAMIL1 and (d) ERA-Interim. Solid lines indicate that evaporation is equal to precipitation, or no vertical motion. Each point represents the annual mean value in one grid box.

needs to be further verified in FAMIL1. We are planning in the next version of FAMIL to employ a two-moment bulk cloud microphysics scheme developed by *Chen and Liu* [2004] to better simulate the aerosol-cloud interaction. With respect to the underestimation of stratocumulus over the eastern ocean, this is a common phenomenon in most AGCMs, and a reliable solution is still lacking. With a single-column simulation of nonprecipitating trade cumulus, *Park and Bretherton* [2009] showed considerable improvements in boundary layer cloud, vertical thermodynamic structure, and less resolution sensitivity in the University of Washington shallow convection (UWShCu) and moist turbulence (UWMT) schemes compared to CAM3.5. In order to improve the simulation of turbulence over the marine stratocumulus region, UWShcu and UWMT schemes are implemented that is a replacement of the current dry turbulence scheme of *Holtslag and Boville* [1993]. On the other hand, as mentioned above, FAMIL1 is designed to be flexible in terms of its resolution, offering a range from 200 to 25 km, and it is important to make the parameterization schemes resolution-adaptive and the related investigation are still ongoing and will be reported in the future.

Another energy bias we could see from Figure 1 is the large TOA imbalance (from 1979 to 2009, the averaged TOA imbalance is approximately 3.8 W m^{-2}). In the current version of FAMIL, we have not tuned any parameter yet. All the parameterizations are originally from SAMIL2 and the publicly released resources (e.g., the dynamic core, Lin microphysics scheme, and the RRTMG radiation scheme) without any tuning. The major modifications of FAMIL1's physical processes are related to the energy and water conservation, which have been already described in Appendix A. We take these modifications as "debugging processes" instead of "tuning parameters". We find this large TOA imbalance mainly comes from the too small FSUT, which may be related to the bias in low-cloud simulation. However, we can achieve TOA balance by adjusting the low-layer entrainment rate in *Tiedtke* [1989] (also the *Nordeng* [1994]) scheme. The entrainment rate was set to 0.3 km^{-1} when there is no large-scale water vapor convergence, much smaller than the values obtained from LES simulations [*Derbyshire et al.*, 2004]. Therefore, we tripled the value to 0.9 km^{-1} (only for low layers). By doing so, we can see the low-clouds increase (see supporting information Figure S5) and the TOA imbalance bias is basically overcome (from 1979 to 2009, the averaged TOA imbalance is less than 0.5 W m^{-2}). For other aspects, generally we saw improved results but no significant differences from the old ones shown in here.
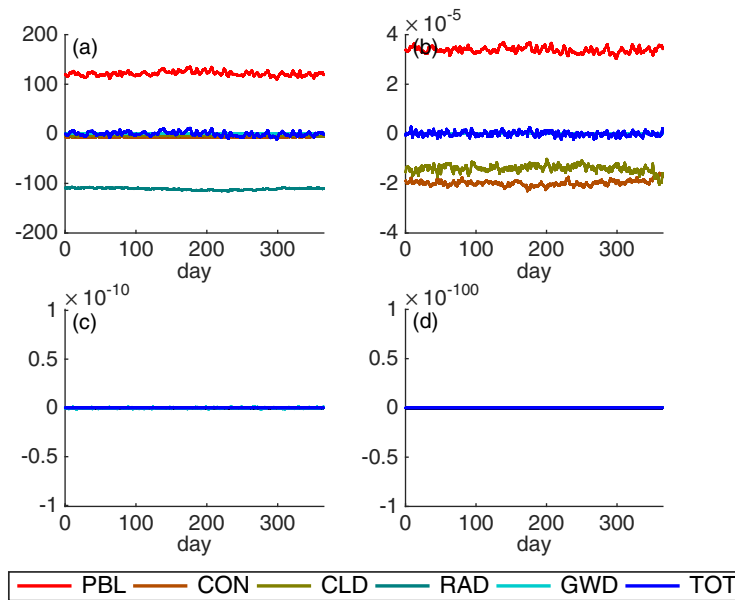
Figure A1. Temporal variation of (a) energy (units: W m^{-2}) and (b) water (units: kg m^{-2} s^{-1}) flux flowing through the boundary of the atmosphere for vertical turbulence (PBL), cumulus convection (CON), cloud microphysics (CLD), radiation (RAD), gravity-wave drag (GWD), and total physics (TOT). Plots (c) and (d) are the difference between energy and water flux flowing through the boundary of the atmosphere and the tendency of vertically integrated energy and water in the atmosphere.

More systematic adjustment in entrainment and detrainment rate will be adopted to further improve the model simulation.

Appendix A

An energy and water conservation-checking module has been designed for each physical parameterization based on the conservation principal: the total energy or water flow through the upper and bottom boundary of the atmosphere should be balanced by the tendency of the vertically integrated total energy or water in the atmosphere. Thus, the conservation relation of energy relation is

$$LH + SH + RF = \frac{\Delta(SE + GE + LE + KE)}{\Delta t} \tag{A1}$$

with units of W m^{-2}, and the conservation relation of water relation is

$$E - P = \frac{\Delta(Qv + Qc + Qr + Qi + Qs + Qg)}{\Delta t} \tag{A2}$$

with units of kg m^{-2} s^{-1}. The items on the left-hand side are: latent heat (LH), sensible heat (SH), radiative fluxes (RF), evaporation (E), and precipitation (P) through the upper or bottom boundary of the atmosphere. The items on the right-hand side are the tendency of the vertically integrated: sensible energy (SE), gravitational-potential energy (GE), latent energy (LE), kinetic energy (KE), water vapor (Qv), cloud water (Qc), rain water (Qr), cloud ice (Qi), snow (Qs), and graupel (Qg) in the atmosphere. Δt is physics time step.

We have made sure that the conservation of energy and water is satisfied for every physical process in each model column at every time step. Take cloud microphysics for example, if there is no energy flowing through the boundary of the atmosphere, then the vertical integrated energy fluxes cancel each other out. Condensation/evaporation of water vapor/cloud water results in heating/cooling in the air. The energy conservation relations in each grid point at each level should follow this transformation relationship: $c_p\Delta T = L_v\Delta Qc = -L_v\Delta Qv$. Where c_p is the specific heat of dry air (J K^{-1} kg^{-1}); L_v is latent heat of vaporization (J kg^{-1}). For water conservation, precipitation through the bottom boundary of the atmosphere produced by cloud microphysics is equal to the tendency of vertical integrated total water constituents in the atmosphere. The misusing of latent heat constants for different kinds of phase change or artificial truncation of species' mass mixing ratio when they are tiny in the cloud microphysics scheme may break the water

conservation in the model. Sometimes negative species will be generated in some extreme conditions that the cloud microphysics scheme failed to consider. Then negative value will be forced to be a small positive value, which again may destroy the energy/water balance. We have assured all these errors not existing in FAMIL1. Similarly we also make sure the energy and water conservation in the cumulus convection scheme. In calculating the vertical diffusion, we switch the diffusion of temperature to diffusion of potential temperature based on the energy conservation. In gravity-wave drag, we take the heating generated by momentum damping into consideration, which was expressed incorrectly before in SAMIL2.

Figure A1 shows that, although different physical processes behave differently in terms of energy and water status and variation, all processes are conserved since total energy and water flux flowing through the upper and bottom boundary of the atmosphere is equal to the tendency of the vertically integrated total energy or water in the atmosphere. The orders of their differences are less than 10^{-10} and 10^{-100} for energy and water, respectively.

References

Adler, R. F., et al. (2003), The version-2 Global Precipitation Climatology Project (GPCP) monthly precipitation analysis (1979-Present), *J. Hydrometeorol.*, *4*(6), 1147–1167, doi:10.1175/1525-7541(2003)004<1147:TVGPCP>2.0.CO;2.

Allan, R. P., C. Liu, N. G. Loeb, M. D. Palmer, M. Roberts, D. Smith, and P.-L. Vidale (2014), Changes in global net radiative imbalance 1985–2012, *Geophys. Res. Lett.*, *41*, 5588–5597, doi:10.1002/2014GL060962.

Allen, M. R., and W. J. Ingram (2002), Constraints on future changes in climate and the hydrologic cycle, *Nature*, *419*(6903), 224–232.

Bao, Q., G. Wu, Y. Liu, J. Yang, Z. Wang, and T. Zhou (2010), An introduction to the coupled model FGOALS1.1-s and its performance in East Asia, *Adv. Atmos. Sci.*, *27*(5), 1131–1142, doi:10.1007/s00376-010-9177-1.

Bao, Q., et al. (2013), The flexible global ocean-atmosphere-land system model, spectral version 2: FGOALS-s2, *Adv. Atmos. Sci.*, *30*(3), 561–576, doi:10.1007/s00376-012-2113-9.

Bechtold, P., N. Semane, P. Lopez, J.-P. Chaboureau, A. Beljaars, and N. Bormann (2013), Representing equilibrium and nonequilibrium convection in large-scale models, *J. Atmos. Sci.*, *71*(2), 734–753, doi:10.1175/JAS-D-13-0163.1.[12226677].

Bengtsson, L. (2010), The global atmospheric water cycle, *Environ. Res. Lett.*, *5*(2), 025202.

Berrisford, P., P. Kållberg, S. Kobayashi, D. Dee, S. Uppala, A. J. Simmons, P. Poli, and H. Sato (2011), Atmospheric conservation properties in ERA-Interim, *Q. J. R. Meteorol. Soc.*, *137*(659), 1381–1399, doi:10.1002/qj.864.

Bodas-Salcedo, A., et al. (2011), COSP: Satellite simulation software for model assessment, *Bull. Am. Meteorol. Soc.*, *92*(8), 1023–1043, doi:10.1175/2011BAMS2856.1.

Chelton, D. B., and F. J. Wentz (2005), Global microwave satellite observations of sea surface temperature for numerical weather prediction and climate research, *Bull. Am. Meteorol. Soc.*, *86*(8), 1097–1115, doi:10.1175/BAMS-86-8-1097.

Chen, J.-P., and S.-T. Liu (2004), Physically based two-moment bulkwater parametrization for warm-cloud microphysics, *Q. J. R. Meteorol. Soc.*, *130*(596), 51–78, doi:10.1256/qj.03.41.

Cionni, I., V. Eyring, J. F. Lamarque, W. J. Randel, D. S. Stevenson, F. Wu, G. E. Bodeker, T. G. Shepherd, D. T. Shindell, and D. W. Waugh (2011), Ozone database in support of CMIP5 simulations: Results and corresponding radiative forcing, *Atmos. Chem. Phys.*, *11*(21), 11267–11292, doi:10.5194/acp-11-11267-2011.

Clough, S. A., M. W. Shephard, E. J. Mlawer, J. S. Delamere, M. J. Iacono, K. Cady-Pereira, S. Boukabara, and P. D. Brown (2005), Atmospheric radiative transfer modeling: A summary of the AER codes, *J. Quant. Spectrosc. Radiat. Transfer*, *91*(2), 233–244, doi:10.1016/j.jqsrt.2004.05.058.

De León, R. R., M. Krämer, D. S. Lee, and J. C. Thelen (2012), Sensitivity of radiative properties of persistent contrails to the ice water path, *Atmos. Chem. Phys.*, *12*(17), 7893–7901, doi:10.5194/acp-12-7893-2012.

Dee, D. P., et al. (2011), The ERA-Interim reanalysis: Configuration and performance of the data assimilation system, *Q. J. R. Meteorol. Soc.*, *137*(656), 553–597, doi:10.1002/qj.828.

Derbyshire, S. H., I. Beau, P. Bechtold, J. Y. Grandpeix, J. M. Piriou, J. L. Redelsperger, and P. M. M. Soares (2004), Sensitivity of moist convection to environmental humidity, *Q. J. R. Meteorol. Soc.*, *130*(604), 3055–3079, doi:10.1256/qj.03.130.

Donner, L. J., et al. (2011), The dynamical core, physical parameterizations, and basic simulation characteristics of the atmospheric component AM3 of the GFDL global coupled model CM3, *J. Clim.*, *24*(13), 3484–3519, doi:10.1175/2011JCLI3955.1.

Dudhia, J. (1989), Numerical study of convection observed during the winter monsoon experiment using a mesoscale two-dimensional model, *J. Atmos. Sci.*, *46*(20), 3077–3107, doi:10.1175/1520-0469(1989)046<3077:NSOCOD>2.0.CO;2.

Edwards, J. M., and A. Slingo (1996), Studies with a flexible new radiation code. I: Choosing a configuration for a large-scale model, *Q. J. R. Meteorol. Soc.*, *122*(531), 689–719, doi:10.1002/qj.49712253107.

Fowler, L. D., D. A. Randall, and S. A. Rutledge (1996), Liquid and ice cloud microphysics in the CSU general circulation model. Part 1: Model description and simulated microphysical processes, *J. Clim.*, *9*(3), 489–529, doi:10.1175/1520-0442(1996)009<0489:LAICMI>2.0.CO;2.

Gates, W. L. (1992), AMIP: The Atmospheric Model Intercomparison Project, *Bull. Am. Meteorol. Soc.*, *73*(12), 1962–1970, doi:10.1175/1520-0477(1992)073<3C1962:ATAMIP>3E2.0.CO;2.

Ghan, S. J., and R. A. Zaveri (2007), Parameterization of optical properties for hydrated internally mixed aerosol, *J. Geophys. Res.*, *112*, D10201, doi:10.1029/2006JD007927.

Harris, L. M., and S.-J. Lin (2014), Global-to-regional nested grid climate simulations in the GFDL high resolution atmospheric model, *J. Clim.*, *27*(13), 4890–4910, doi:10.1175/JCLI-D-13-00596.1.

Hartmann, D. L. (1994), *Global Physical Climatology*, X, 411 pp., Academic, N. Y.

Holtslag, A. A. M., and B. A. Boville (1993), Local versus nonlocal boundary-layer diffusion in a global climate model, *J. Clim.*, *6*(10), 1825–1842, doi:10.1175/1520-0442(1993)006<1825:LVNBLD>2.0.CO;2.

Hong, S.-Y., J. Dudhia, and S.-H. Chen (2004), A revised approach to ice microphysical processes for the bulk parameterization of clouds and precipitation, *Mon. Weather Rev.*, *132*(1), 103–120, doi:10.1175/1520-0493(2004)132<0103:ARATIM>2.0.CO;2.

Huang, Y., R. E. Dickinson, and W. L. Chameides (2006), Impact of aerosol indirect effect on surface temperature over East Asia, *Proc. Natl. Acad. Sci. U. S. A.*, *103*(12), 4371–4376, doi:10.1073/pnas.0504428103.

Huffman, G. J., R. F. Adler, M. M. Morrissey, D. T. Bolvin, S. Curtis, R. Joyce, B. McGavock, and J. Susskind (2001), Global precipitation at one-degree daily resolution from multisatellite observations, *J. Hydrometeorol.*, *2*(1), 36–50, doi:10.1175/1525-7541(2001)002<0036:GPAODD>2.0.CO;2.

Huffman, G. J., D. T. Bolvin, E. J. Nelkin, D. B. Wolff, R. F. Adler, G. Gu, Y. Hong, K. P. Bowman, and E. F. Stocker (2007), The TRMM Multisatellite Precipitation Analysis (TMPA): Quasi-global, multiyear, combined-sensor precipitation estimates at fine scales, *J. Hydrometeorol.*, *8*(1), 38–55, doi:10.1175/JHM560.1.

Hurrell, J. W., J. J. Hack, D. Shea, J. M. Caron, and J. Rosinski (2008), A new sea surface temperature and sea ice boundary dataset for the community atmosphere model, *J. Clim.*, *21*(19), 5145–5153, doi:10.1175/2008JCLI2292.1.

Hwang, Y.-T., and D. M. W. Frierson (2013), Link between the double-intertropical convergence zone problem and cloud biases over the Southern Ocean, *Proc. Natl. Acad. Sci. U. S. A.*, *110*(13), 4935–4940, doi:10.1073/pnas.1213302110.

Karl, T. R., and K. E. Trenberth (2003), Modern global climate change, *Science*, *302*(5651), 1719–1723.

Kiehl, J. T., and K. E. Trenberth (1997), Earth's annual global mean energy budget, *Bull. Am. Meteorol. Soc.*, *78*(2), 197–208, doi:10.1175/1520-0477(1997)078<0197:EAGMEB>2.0.CO;2.

Klein, S. A., and C. Jakob (1999), Validation and sensitivities of frontal clouds simulated by the ECMWF model, *Mon. Weather Rev.*, *127*(10), 2514–2531, doi:10.1175/1520-0493(1999)127<2514:VASOFC>2.0.CO;2.

Lamarque, J. F., et al. (2010), Historical (1850–2000) gridded anthropogenic and biomass burning emissions of reactive gases and aerosols: Methodology and application, *Atmos. Chem. Phys.*, *10*(15), 7017–7039, doi:10.5194/acp-10-7017-2010.

Lamarque, J. F., et al. (2012), CAM-chem: Description and evaluation of interactive atmospheric chemistry in the Community Earth System Model, *Geosci. Model Dev.*, *5*(2), 369–411, doi:10.5194/gmd-5-369-2012.

Lin, S.-J. (2004), A "Vertically Lagrangian" finite-volume dynamical core for global models, *Mon. Weather Rev.*, *132*(10), 2293–2307, doi:10.1175/1520-0493(2004)132%3C2293:AVLFDC%3E2.0.CO;2.

Lin, S.-J., and R. B. Rood (1996), Multidimensional flux-form semi-Lagrangian transport schemes, *Mon. Weather Rev.*, *124*(9), 2046–2070, doi:10.1175/1520-0493(1996)124%3C2046:MFFSLT%3E2.0.CO;2.

Lin, Y.-L., R. D. Farley, and H. D. Orville (1983), Bulk parameterization of the snow field in a cloud model, *J. Clim. Appl. Meteor.*, *22*(6), 1065–1092, doi:10.1175/1520-0450(1983)022<1065:BPOTSF>2.0.CO;2.

Lin, S.-J., W. Chao, Y. C. Sud, and G. K. Walker (1994), A class of the van Leer-type transport schemes and its application to the moisture transport in a general circulation model, *Mon. Weather Rev.*, *122*(7), 1575–1593, doi:10.1175/1520-0493(1994)122%3C1575:ACOTVL%3E2.0.CO;2.

Liu, X., et al. (2012), Toward a minimal representation of aerosols in climate models: Description and evaluation in the Community Atmosphere Model CAM5, *Geosci. Model Dev.*, *5*(3), 709–739, doi:10.5194/gmd-5-709-2012.

Loeb, N. G., B. A. Wielicki, D. R. Doelling, G. L. Smith, D. F. Keyes, S. Kato, N. Manalo-Smith, and T. Wong (2009), Toward optimal closure of the earth's top-of-atmosphere radiation budget, *J. Clim.*, *22*(3), 748–766, doi:10.1175/2008JCLI2637.1.

Lu, J., and M. Cai (2009), Stabilization of the atmospheric boundary layer and the muted global hydrological cycle response to global warming, *J. Hydrometeorol.*, *10*(1), 347–352, doi:10.1175/2008JHM1058.1.

Meinshausen, M., et al. (2011), The RCP greenhouse gas concentrations and their extensions from 1765 to 2300, *Clim. Change*, *109*(1–2), 213–241, doi:10.1007/s10584-011-0156-z.

Morrison, H., J. A. Curry, and V. I. Khvorostyanov (2005), A new double-moment microphysics parameterization for application in cloud and climate models. Part I: Description, *J. Atmos. Sci.*, *62*(6), 1665–1677, doi:10.1175/JAS3446.1.

Neale, R. B., J. Richter, S. Park, P. H. Lauritzen, S. J. Vavrus, P. J. Rasch, and M. Zhang (2013), The mean climate of the Community Atmosphere Model (CAM4) in forced SST and fully coupled experiments, *J. Clim.*, *26*(14), 5150–5168, doi:10.1175/JCLI-D-12-00236.1.

Nordeng, T. E. (1994), *Extended Versions of the Convective Parametrization Scheme at ECMWF and Their Impact on the Mean and Transient Activity of the Model in the Tropics*, Eur. Cent. Medium Range Weather Forecasts, Reading.

Ohmura, A., and M. Wild (2002), Is the hydrological cycle accelerating?, *Science*, *298*(5597), 1345–1346, doi:10.1126/science.1078972.

Palmer, T. N., G. J. Shutts, and R. Swinbank (1986), Alleviation of a systematic westerly bias in general circulation and numerical weather prediction models through an orographic gravity wave drag parametrization, *Q. J. R. Meteorol. Soc.*, *112*(474), 1001–1039, doi:10.1002/qj.49711247406.

Park, S., and C. S. Bretherton (2009), The University of Washington shallow convection and moist turbulence schemes and their impact on climate simulations with the Community Atmosphere Model, *J. Clim.*, *22*(12), 3449–3469, doi:10.1175/2008JCLI2557.1.

Pincus, R., H. W. Barker, and J.-J. Morcrette (2003), A fast, flexible, approximate technique for computing radiative transfer in inhomogeneous cloud fields, *J. Geophys. Res.*, *108*(D13), 4376, doi:10.1029/2002JD003322.

Popke, D., B. Stevens, and A. Voigt (2013), Climate and climate change in a radiative-convective equilibrium version of ECHAM6, *J. Adv. Model. Earth Syst.*, *5*(1), 1–14, doi:10.1029/2012MS000191.

Putman, W. M., and S.-J. Lin (2007), Finite-volume transport on various cubed-sphere grids, *J. Comput. Phys.*, *227*(1), 55–78, doi:10.1016/j.jcp.2007.07.022.

Ramanathan, V. (1987), The role of earth radiation budget studies in climate and general circulation research, *J. Geophys. Res.*, *92*(D4), 4075–4095, doi:10.1029/JD092iD04p04075.

Ramanathan, V., P. J. Crutzen, J. T. Kiehl, and D. Rosenfeld (2001), Aerosols, climate, and the hydrological cycle, *Science*, *294*(5549), 2119–2124, doi:10.1126/science.1064034.

Rienecker, M. M., et al. (2011), MERRA: NASA's modern-era retrospective analysis for research and applications, *J. Clim.*, *24*(14), 3624–3648, doi:10.1175/JCLI-D-11-00015.1.

Rutledge, S. A., and P. V. Hobbs (1984), The mesoscale and microscale structure and organization of clouds and precipitation in midlatitude cyclones. XII: A diagnostic modeling study of precipitation development in narrow cold-frontal rainbands, *J. Atmos. Sci.*, *41*(20), 2949–2972, doi:10.1175/1520-0469(1984)041<2949:TMAMSA>2.0.CO;2.

Stephens, G. L., J. Li, M. Wild, C. A. Clayson, N. Loeb, S. Kato, T. L'Ecuyer, P. W. Stackhouse, M. Lebsock, and T. Andrews (2012), An update on Earth's energy balance in light of the latest global observations, *Nat. Geosci.*, *5*(10), 691–696.

Stevens, B., and S. Schwartz (2012), Observing and modeling earth's energy flows, *Surv. Geophys.*, *33*(3–4), 779–816, doi:10.1007/s10712-012-9184-0.

Subin, Z. M., W. J. Riley, J. Jin, D. S. Christianson, M. S. Torn, and L. M. Kueppers (2010), Ecosystem feedbacks to climate change in California: Development, testing, and analysis using a coupled regional atmosphere and land surface model (WRF3–CLM3.5), *Earth Interact.*, *15*(15), 1–38, doi:10.1175/2010EI331.1.

Sun, Z. (2011), Improving transmission calculations for the Edwards–Slingo radiation scheme using a correlated-k distribution method, *Q. J. R. Meteorol. Soc.*, *137*(661), 2138–2148, doi:10.1002/qj.880.

Taylor, K. E. (2001), Summarizing multiple aspects of model performance in a single diagram, *J. Geophys. Res.*, *106*(D7), 7183–7192, doi:10.1029/2000JD900719.

Tiedtke, M. (1989), A comprehensive mass flux scheme for cumulus parameterization in large-scale models, *Mon. Weather Rev.*, *117*(8), 1779–1800, doi:10.1175/1520-0493(1989)117<1779:ACMFSF>2.0.CO;2.

Trenberth, K. E., J. T. Fasullo, and J. Kiehl (2009), Earth's global energy budget, *Bull. Am. Meteorol. Soc.*, *90*(3), 311–323, doi:10.1175/2008BAMS2634.1.

Trenberth, K. E., J. T. Fasullo, and J. Mackaro (2011), Atmospheric moisture transports from ocean to land and global energy flows in reanalyses, *J. Clim.*, *24*(18), 4907–4924, doi:10.1175/2011JCLI4171.1.

Waliser, D., K. W. Seo, S. Schubert, and E. Njoku (2007), Global water cycle agreement in the climate models assessed in the IPCC AR4, *Geophys. Res. Lett.*, *34*, L16705, doi:10.1029/2007GL030675.

Wang, X., and M. Zhang (2013), An analysis of parameterization interactions and sensitivity of single-column model simulations to convection schemes in CAM4 and CAM5, *J. Geophys. Res.*, *118*, 8869–8880, doi:10.1002/jgrd.50690.

Wang, X., Y. Liu, Q. Bao, and Z. Wang (2012), Climate sensitivity and cloud feedback processes imposed by two different external forcings in an aquaplanet GCM, *Theor. Appl. Climatol.*, *110*(1–2), 1–10, doi:10.1007/s00704-012-0607-0.

Wang, X., Y. Liu, G. Wu, S.-J. Lin, and Q. Bao (2013), The application of flux-form semi-Lagrangian transport scheme in a spectral atmosphere model, *Adv. Atmos. Sci.*, *30*(1), 89–100, doi:10.1007/s00376-012-2039-2.

Wang, Z., G. Wu, T. Wu, and R. Yu (2004), Simulation of Asian monsoon seasonal variations with climate model R42L9/LASG, *Adv. Atmos. Sci.*, *21*(6), 879–889, doi:10.1007/BF02915590.

Wild, M. (2012), New directions: A facelift for the picture of the global energy balance, *Atmos. Environ.*, *55*, 366–367, doi:10.1016/j.atmosenv.2012.03.022.

Wild, M., and B. Liepert (2010), The Earth radiation balance as driver of the global hydrological cycle, *Environ. Res. Lett.*, *5*(2), 025203.

Wild, M., D. Folini, C. Schär, N. Loeb, E. Dutton, and G. König-Langlo (2013), The global energy balance from a surface perspective, *Clim. Dyn.*, *40*(11–12), 3107–3134, doi:10.1007/s00382-012-1569-8.

Wu, G., H. Liu, Y. Zhao, and W. Li (1996), A nine-layer atmospheric general circulation model and its performance, *Adv. Atmos. Sci.*, *13*(1), 1–18, doi:10.1007/BF02657024.

Wu, T., P. Liu, Z. Wang, Y. Liu, R. Yu, and G. Wu (2003), The performance of atmospheric component model R42L9 of GOALS/LASG, *Adv. Atmos. Sci.*, *20*(5), 726–742, doi:10.1007/BF02915398.

Xie, P., and P. A. Arkin (1997), Global precipitation: A 17-year monthly analysis based on gauge observations, satellite estimates, and numerical model outputs, *Bull. Am. Meteorol. Soc.*, *78*(11), 2539–2558, doi:10.1175/1520-0477(1997)078<2539:GPAYMA>2.0.CO;2.

Xie, S., and M. Zhang (2000), Impact of the convection triggering function on single-column model simulations, *J. Geophys. Res.*, *105*(D11), 14983–14996, doi:10.1029/2000JD900170.

Xu, K.-M., and D. A. Randall (1996), A semiempirical cloudiness parameterization for use in climate models, *J. Atmos. Sci.*, *53*(21), 3084–3102, doi:10.1175/1520-0469(1996)053<3084:ASCPFU>2.0.CO;2.

Yang, J., Q. Bao, and X. Wang (2013), Intensified eastward and northward propagation of tropical intraseasonal oscillation over the equatorial Indian Ocean in a global warming scenario, *Adv. Atmos. Sci.*, *30*(1), 167–174, doi:10.1007/s00376-012-1260-3.

Yu, L., and R. A. Weller (2007), Objectively analyzed air–sea heat fluxes for the global ice-free oceans (1981–2005), *Bull. Am. Meteorol. Soc.*, *88*(4), 527–539, doi:10.1175/BAMS-88-4-527.

Zhang, G. J. (2002), Convective quasi-equilibrium in midlatitude continental environment and its effect on convective parameterization, *J. Geophys. Res.*, *107*(D14), 4220, doi:10.1029/2001JD001005.

Zhang, Y., W. B. Rossow, and P. W. Stackhouse (2007), Comparison of different global information sources used in surface radiative flux calculation: Radiative properties of the surface, *J. Geophys. Res.*, *112*, D01102, doi:10.1029/2005JD007008.

Zhou, L., Y. Liu, Q. Bao, H. Yu, and G. Wu (2012), Computational performance of the high-resolution atmospheric model FAMIL, *Atmos. Oceanic Sci. Lett.*, *5*(5), 355–359.